EFFECT OF THE GROWTH RATE ON THE MICROSTRUCTURE AND ROOM-TEMPERATURE TENSILE PROPERTIES OF DIRECTIONALLY SOLIDIFIED Ni_3Al-BASED IN-SITU COMPOSITES

JURAJ LAPIN*, OTO BAJANA

Institute of Materials and Machine Mechanics, Slovak Academy of Sciences, Račianska 75, 831 02 Bratislava, Slovak Republic

Received 4 February 2005, accepted 8 February 2005

Effect of the growth rate on the microstructure and room-temperature tensile properties of two directionally solidified (DS) Ni_3Al-based in-situ composites with the chemical compositions Ni-20.2Mo-14.1Al-3.6Cr and Ni-20.4Mo-14.7Al-1.8V [at.%] was studied. Directional solidification was performed in a Bridgman apparatus at constant growth rates R ranging from 1.39×10^{-6} to 11.1×10^{-6} $m \cdot s^{-1}$ and a constant temperature gradient in liquid at the solid liquid of $G_L = 15 \times 10^3$ $K \cdot m^{-1}$. Increase of the growth rate leads to a decrease of interfibre spacing λ according to a relationship $\lambda = K_1 R^{-0.5}$, where a material constant K_1 for both alloys is determined to be 4.44×10^{-9} $m^{1.5} \cdot s^{-0.5}$. The growth rates of 6.94×10^{-6} and 8.33×10^{-6} $m \cdot s^{-1}$ are found to be critical for a planar front solidification for the alloy modified by chromium and vanadium, respectively. At higher growth rates, a breakdown of planar front solidification is observed. For the composites with a perfect aligned fibre structure, the yield stress of the composites increases with increasing growth rate. Formation of cellular structure results in a decrease of the yield stress and ultimate tensile strength. A model predicting the offset yield stress of the composites in relation to their microstructural variables is proposed.

K e y w o r d s: Ni_3Al, in-situ composites, microstructure, directional solidification, tensile properties

1. Introduction

Multiphase intermetallic alloys based on Ni_3Al or NiAl are potential materials for high-temperature structural applications. These alloys can provide a good combination of room-temperature tensile ductility, oxidation resistance, strength and creep resistance that cannot be achieved in monolithic intermetallics [1–7]. The

*corresponding author, e-mail: ummslapi@savba.sk

basic idea of multiphase in-situ composites is to include a metallic phase for improved room temperature toughness and number of intermetallic phases for good high temperature properties [8, 9]. An advantage of producing in-situ composites from eutectic Ni_3Al or NiAl based alloys is that coexisting phases are thermodynamically stable up to melting point. The disadvantages of working with eutectic alloys are the limited composition ranges where couple growth of phases may take place, and morphological instabilities of the reinforcing phases during long-term thermo-mechanical loading. In addition, the phase diagrams of some ternary and majority of quaternary or higher alloy systems are unknown, which causes difficulties in further optimization of their chemical composition for a specific structural application.

Among various eutectic alloys, large research effort was devoted to directionally solidified (DS) Ni_3Al-based in-situ composites reinforced by molybdenum fibres [10–15]. Earlier works on these alloys have shown that variations in the cross-sectional area of growing composite cause local changes in growth rate (R), temperature gradient in the liquid at the solid-liquid interface (G_L) and curvature of the solid-liquid interface [16, 17]. Changes in the growth rate lead to variation in interfibre spacing and fibre diameter, which can significantly affect local mechanical properties of DS components.

The aim of this paper is to study the effect of the growth rate on the microstructure and room-temperature tensile properties of two DS Ni_3Al-based in-situ composites. In this study, basic eutectic Ni-20.1Mo-13.6Al [at.%] alloy described elsewhere [18] is modified by additions of chromium and vanadium to improve its high-temperature oxidation resistance and strength, respectively.

2. Experimental procedure

Master ingots of the eutectic alloys with the chemical composition given in Table 1 were prepared in a vacuum induction furnace by melting high-purity metals in argon atmosphere and casting into a copper chill mould. These ingots were machined to rods and placed into high purity alumina cylindrical moulds with an inner diameter of 12 mm. Directional solidification was performed under argon atmosphere in a modified Bridgman-type solidification apparatus described elsewhere [19]. This apparatus is based on withdrawing a mould containing the molten alloy from resistance furnace through a water-cooled copper chill. All specimens were prepared using constant growth rates ranging from 1.39×10^{-6} to $11.1 \times$

Table 1. Chemical composition of Ni_3Al-based eutectic alloys [at.%]

	Ni	Mo	Al	Cr	V	C	W	S
Alloy 1	Bal.	20.19	14.13	3.55	–	0.026	0.002	0.002
Alloy 2	Bal.	20.39	14.69	–	1.81	0.051	0.002	0.002

$\times 10^{-6}$ m·s^{-1} and a constant temperature gradient in liquid at the solid/liquid interface of $G_L = 15 \times 10^3$ K·m^{-1}. The temperature gradient G_L was measured using PtRh6-PtRh30 thermocouple (1.5 mm outside tube diameter) placed along the axis of the crucible. The degree of fibre alignment was metallographically determined by grinding and polishing a longitudinal flat along the DS bars. After directional solidification the ingots were annealed at 1123 K for 100 h under argon atmosphere.

Cylindrical tensile specimens with a gauge length of 28 mm and a gauge diameter of 4 mm were lathe-machined only from fully fibre-aligned sections of the annealed ingots. The tensile axis of the specimens was parallel to the growth direction of the fibres. Tensile tests were performed on a universal Instron machine at an initial strain rate of 1.67×10^{-3} s^{-1}.

The microstructure of in-situ composites was studied using optical microscopy (OM) and scanning electron microscopy (SEM). The interfibre spacing λ was calculated from measured values of fibre density ρ (number of fibres per unit area) according to Thompson relationship [20]

$$\lambda = 1.075 \frac{1}{\sqrt{\rho}} \, . \tag{1}$$

3. Results and discussion

3.1 Microstructure

Figure 1 shows the typical as-cast microstructure of the Alloy 1. After directional solidification at a planar solid-liquid interface a regular in-situ fibre structure is formed, as shown in Fig. 2. As seen in this figure, the microstructure on a transverse section consists of square shaped α-fibres (Mo-based solid solution with bcc crystal structure). The fibres are surrounded with intermetallic γ'-phase (Ni_3Al phase with $L1_2$ crystal structure). Between the γ'-regions, irregular regions of γ-phase (Ni-based solid solution with fcc crystal structure) are formed. Both the fibres and matrix grow in $\langle 100 \rangle$ growth direction with $\{100\}_{\gamma/\gamma'} \| \{110\}_{\alpha}$ crystallographic relationship [12, 13]. Using image analysis, volume fraction of reinforcing fibres V_f was determined to be 25.5 and 24.5 vol.% for the Alloy 1 and Alloy 2, respectively. Table 2 summarizes measured microstructural parameters including interfibre spacing λ, free fibre spacing L and equivalent fibre diameter d.

The measured interfibre spacing λ and corresponding growth rates R were fitted to the well-known relationship [21]

$$\lambda = K_1 \frac{1}{\sqrt{R}}, \tag{2}$$

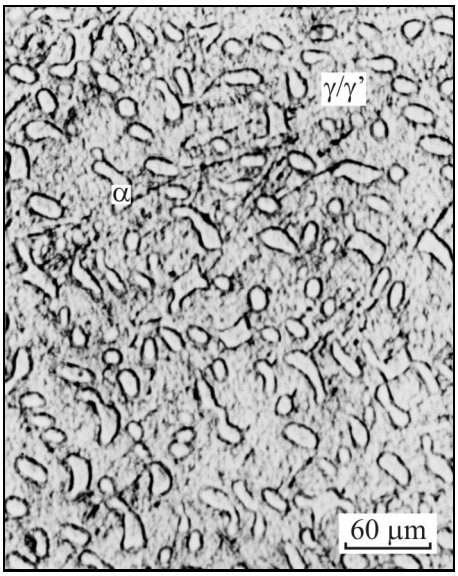

Fig. 1. Optical micrograph showing the typical as-cast microstructure of the Alloy 1.

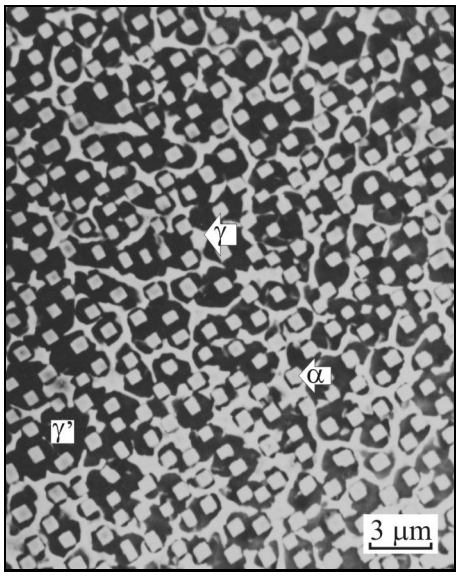

Fig. 2. SEM micrograph showing the typical square morphology of reinforcing fibres on a transverse section of DS Ni_3Al-based in-situ composites, $R = 4.17 \times 10^{-6}$ m·s^{-1}.

Table 2. Variations of the interfibre spacing λ, free fibre spacing L and fibre diameter d with the growth rate R

Growth rate R [10^{-6} m·s^{-1}]	Interfibre spacing λ [10^{-6} m]		Fibre spacing L [10^{-6} m]		Equivalent fibre diameter d [10^{-6} m]	
	Alloy 1	Alloy 2	Alloy 1	Alloy 2	Alloy 1	Alloy 2
1.39	3.72	3.91	1.89	1.83	1.83	2.08
2.78	2.73	2.63	1.38	1.24	1.35	1.39
4.17	2.15	2.11	1.09	0.99	1.06	1.12
5.56	1.87	1.79	0.95	0.84	0.92	0.95
6.94	1.68	1.65	0.85	0.77	0.83	0.88
8.33	Cells	1.48	Cells	0.69	Cells	0.79
11.10	Cells	Cells	Cells	Cells	Cells	Cells

where K_1 is a material constant. Figure 3 graphically summarizes the dependence of the interfibre spacing on the growth rate. Using linear regression analysis, the material constant is calculated to be $K_1 = 4.44 \times 10^{-9}$ m$^{1.5}$·s$^{-0.5}$. The corre-

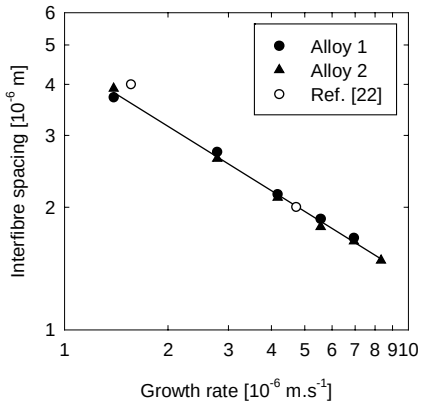

Fig. 3. Variation of the interfibre spacing with the steady-state growth rate.

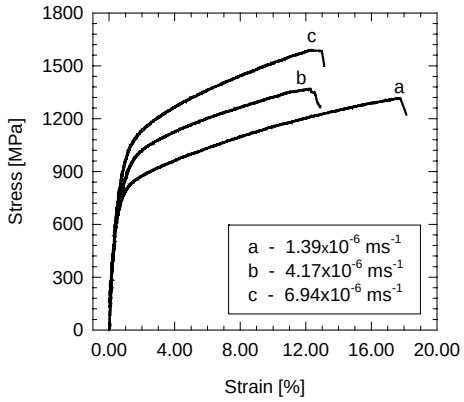

Fig. 4. Room-temperature tensile stress-strain curves of DS in-situ composite (Alloy 1). Growth rates are indicated in the figure.

lation coefficient r^2 of this fit is 0.99. Comparison of the present data with the results reported by Whittenberger and Wirth [22] for an alloy of similar chemical composition indicates a good correlation among these alloys.

The growth of in-situ composites with well-aligned fibre structure requires fulfilling constitutional super-cooling criterion for plane front solidification defined as [23]

$$\left(\frac{G_{\mathrm{L}}}{R}\right) \geq \frac{\Delta T}{D}, \tag{3}$$

where ΔT is the freezing temperature range of the alloy and D is the diffusion coefficient in the liquid. The growth rates of 6.94×10^{-6} and 8.33×10^{-6} m·s^{-1} are found to be critical for a planar front solidification at a constant temperature gradient of $G_{\mathrm{L}} = 15 \times 10^3$ K·m^{-1} for the Alloy 1 and Alloy 2, respectively. At higher growth rates a breakdown of planar front solidification resulting in the growth of irregular eutectic structure is observed. The critical values of $(G_{\mathrm{L}}R^{-1})_{\mathrm{crit}}$ at which the breakdown of planar solid-liquid interface is observed are determined to be 21.6×10^8 and 18×10^8 K·s·m^{-2} for the Alloy 1 and Alloy 2, respectively. These values are comparable with a value of 18×10^8 K·s·m^{-2} previously reported by Pelachová and Kováčová [13] for in-situ composites with similar chemical compositions.

3.2 Room-temperature tensile properties

Figure 4 shows the typical room-temperature tensile stress-strain curves for

Table 3. Variations of the yield stress (σ_y), ultimate tensile stress and elongation with the growth rate R for DS Alloy 1 and Alloy 2

Growth rate R [10^{-6} m·s^{-1}]	Yield stress σ_y [MPa]		Ultimate tensile stress [MPa]		Elongation [%]	
	Alloy 1	Alloy 2	Alloy 1	Alloy 2	Alloy 1	Alloy 2
1.39	642	510	1317	1130	17.7	12.2
2.78	658	540	1358	1130	15.1	8.3
4.17	676	560	1370	1260	12.3	11.1
5.56	689	570	1452	1190	11.8	9.4
6.94	707	585	1538	1205	13.0	8.8
8.33	680	605	1403	1245	12.6	9.2
11.10	620	–	1416	–	12.3	–

the Alloy 1. Both composites showed smooth yielding without any discontinuities. Table 3 summarizes the measured values of 0.2% offset yield stress (σ_y), ultimate tensile stress and elongation as a function of the growth rate. It should be noted that the data shown in this table represent the average values from four tensile specimens tested at each growth rate. The increase of the growth rate results in an increase of the yield stress. For both alloys the highest tensile ductility was measured at the lowest growth rate of 1.39×10^{-6} m·s^{-1}. Formation of eutectic cells at high growth rates results in a decrease of the yield stress and ultimate tensile strength.

The increase of the yield stress with the increasing growth rate of in-situ composite with an aligned fibre microstructure might be explained by the changes of the microstructural parameters (interfibre spacing, fibre spacing, fibre diameter and volume fraction of the reinforcing fibres). Figure 5 illustrates some basic assumption for analytical estimation of the offset yield stress σ_y from the tensile curve of the eutectic composite. We assume that for aligned fibre composites stressed along the fibre direction, the straining within the composite is uniform. At the offset plastic strain ε^*, we assume only elastic deformation of the fibres and plastic deformation of the matrix. Due to large aspect ratio of the α-reinforcing phase and low temperature, the dislocations within the γ/γ'-matrix are unlikely to be able to bypass the fibres by climb. Thus bypass occurs by Orowan bowing leaving dislocation loops around the fibres. Assuming crystallographic features of the slip systems in the studied in-situ composites, the Orowan bowing stress σ_{OR} can be calculated as [24]

$$\sigma_{OR} = a\frac{G_m b_m}{\pi L}\ln\frac{d}{2r}, \tag{4}$$

where a is a constant, G_m is the matrix shear modulus in the slip direction, b_m is the length of the matrix Burgers vector, L is the free fibre spacing, d is the fibre

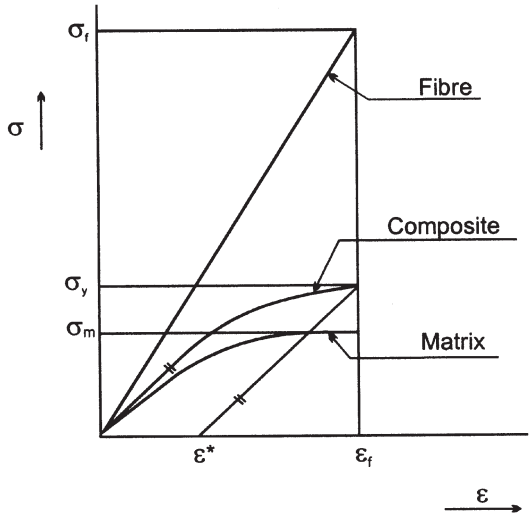

Fig. 5. Partitioning of the stresses between the fibres and matrix at the offset yield strain ε^*.

diameter and r is the inner cut-off radius of the dislocations. The constant a is equal to 1.32 for the slip on the octahedral {111} slip planes and in ⟨110⟩ slip directions (slip systems operating preferentially at low temperature) and to 1.08 for the slip on {101} slip planes and in ⟨110⟩ slip directions (addition operating slip systems at high temperatures) [24].

The offset yield stress σ_{y} of the composite can be estimated using the rule of mixtures which yields

$$\sigma_{\mathrm{y}} = \sigma_{\mathrm{f}} V_{\mathrm{f}} + \sigma_{\mathrm{m}} \left(1 - V_{\mathrm{f}}\right), \tag{5}$$

where σ_{f} is the stress carried by the fibres, σ_{m} $(= \sigma_{\mathrm{mo}} + \sigma_{\mathrm{OR}})$ is the stress carried by the matrix and σ_{mo} is the reference stress that would be carried by the matrix without the reinforcing fibres. At the offset yield stress σ_{y}, the stress carried by the fibres can be expressed as

$$\sigma_{\mathrm{f}} = E_{\mathrm{f}} \varepsilon_{\mathrm{f}}, \tag{6}$$

where E_{f} is the elastic modulus of fibres. The strain ε_{f} can be estimated in the form

$$\varepsilon_{\mathrm{f}} = \varepsilon^* + \frac{\sigma_{\mathrm{y}}}{E_{\mathrm{c}}}, \tag{7}$$

where ε^* is the offset yield strain and E_{c} is the elastic modulus of the composite.

Taking into account Eq. (7), Eq. (5) can be rewritten in the form

$$\sigma_{\mathrm{y}} = E_{\mathrm{f}} V_{\mathrm{f}} \left(\varepsilon^* + \frac{\sigma_{\mathrm{y}}}{E_{\mathrm{c}}} \right) + (\sigma_{\mathrm{mo}} + \sigma_{\mathrm{OR}}) (1 - V_{\mathrm{f}}) , \tag{8}$$

or in the form

$$\sigma_{\mathrm{y}} = A (\sigma_{\mathrm{mo}} + \sigma_{\mathrm{OR}}) + B, \tag{9}$$

where constants A and B are defined as

$$A = \frac{E_{\mathrm{c}} (1 - V_{\mathrm{f}})}{E_{\mathrm{c}} - E_{\mathrm{f}} V_{\mathrm{f}}}, \tag{10}$$

$$B = A \frac{\varepsilon^* E_{\mathrm{f}} V_{\mathrm{f}}}{1 - V_{\mathrm{f}}}. \tag{11}$$

Table 4 summarizes the results of calculations of different stresses at the offset yield stress for both composites. In this table, the Orowan stresses were calculated taking value of $a = 1.32$, $G_{\mathrm{m}} = 65.1$ GPa for the matrix shear stress [25], $r = 0.5 b_{\mathrm{m}}$ and $b_{\mathrm{m}} = 5.08 \times 10^{-10}$ m for the Burgers vector of the γ' superdislocation [26]. The matrix reference stresses σ_{mo} were calculated from Eq. (8) taking value of $E_{\mathrm{c}} =$ 174 GPa for the Young's modulus of the composite, $E_{\mathrm{f}} = 300$ GPa for the Young's modulus of the molybdenum fibres and $\varepsilon^* = 0.002$ for the offset yield strain. The results of these calculations are graphically summarized in Figs. 6a and 6b. As can be concluded from these figures, the reference matrix stress is nearly constant for all growth rates. Apparently low values of σ_{mo} at which the matrix should yield are comparable with the room-temperature yield stresses observed for several single

Table 4. Calculated values of Orowan stress σ_{OR}, reference matrix stress σ_{mo}, matrix stress σ_{m} and fibre stress σ_{f} as functions of the growth rate R

Growth rate R [10^{-6} m·s^{-1}]	Orowan stress σ_{OR} [MPa]		Reference matrix stress σ_{mo} [MPa]		Matrix stress σ_{m} [MPa]		Fibre stress σ_{f} [MPa]	
	Alloy 1	Alloy 2	Alloy 1	Alloy 2	Alloy 1	Alloy 2	Alloy 1	Alloy 2
1.39	55.1	57.9	241.0	137.5	277.5	195.4	1707	1493
2.78	72.4	81.0	236.2	137.4	289.5	218.4	1734	1531
4.17	88.6	98.4	233.8	135.5	303.1	233.7	1766	1566
5.56	99.6	113.2	232.8	128.1	312.8	241.4	1788	1583
6.94	109.7	122.1	236.5	130.7	326.4	252.8	1819	1609
8.33	–	134.1	–	134.0	–	268.1	–	1643

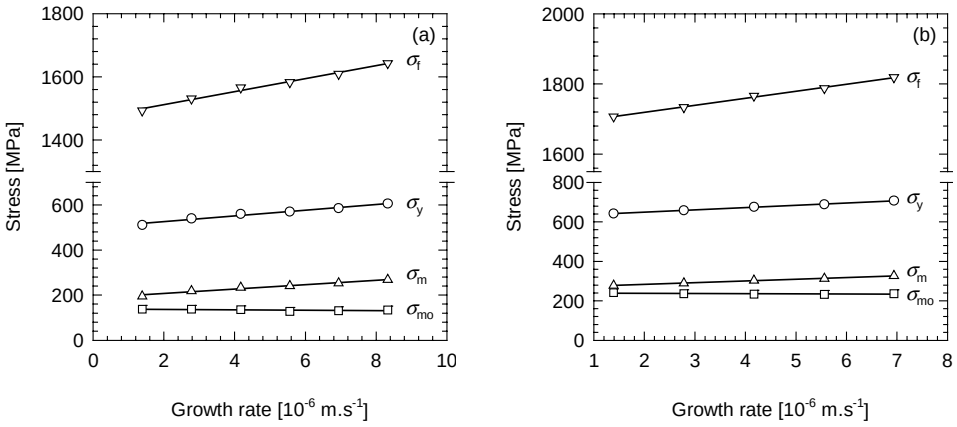

Fig. 6. Dependences of the yield stress σ_{y}, reference matrix stress σ_{mo}, matrix stress σ_{m} and fibre stress σ_{f} on the growth rate: (a) Alloy 1; (b) Alloy 2.

phase Ni_3Al alloys and nickel based solid solutions [27–29]. It should be noted that the matrix of the in-situ composites contains about 75 vol.% of Ni_3Al (γ'-phase) and 25 vol.% of Ni-based solid solution (γ-phase). Since the γ'-phase forms continuous layer around α-Mo fibres and γ-phase is found in the form of relatively large regions separating the γ'-phase, the reference yield stress of the matrix resulting from our calculation seems to be reasonable for the studied alloys. It seems also reasonable that the fine single crystalline α-fibres (whiskers) with nearly perfect crystal structure might carry such high elastic stresses without yielding. Recently the high-resolution electron microscopy studies revealed precipitation strengthening of the α-phase by fine Ni_3Mo and Ni_3Al particles in heat-treated composites [30, 31], which supports high calculated stress values carried by the fibres at the offset yield point of the composites.

3.3 Tensile fracture

The initiation of the fracture cracks occurred at the surface in the macroscopically necked regions of the tensile specimens. Figure 7a shows typical palisade fracture surface. As seen in this figure, numerous cracks parallel to the stress axis of the specimens are formed. Some of these cracks propagate along the columnar eutectic grain boundaries and some within the eutectic grains along the fibre-matrix interfaces in a direction parallel to the stress axis. Metallographic observations revealed that the reinforcing fibres deformed plastically without any evidence for cracking or fragmentation (Fig. 7b). As seen in Figs. 7c and 7d, both the matrix

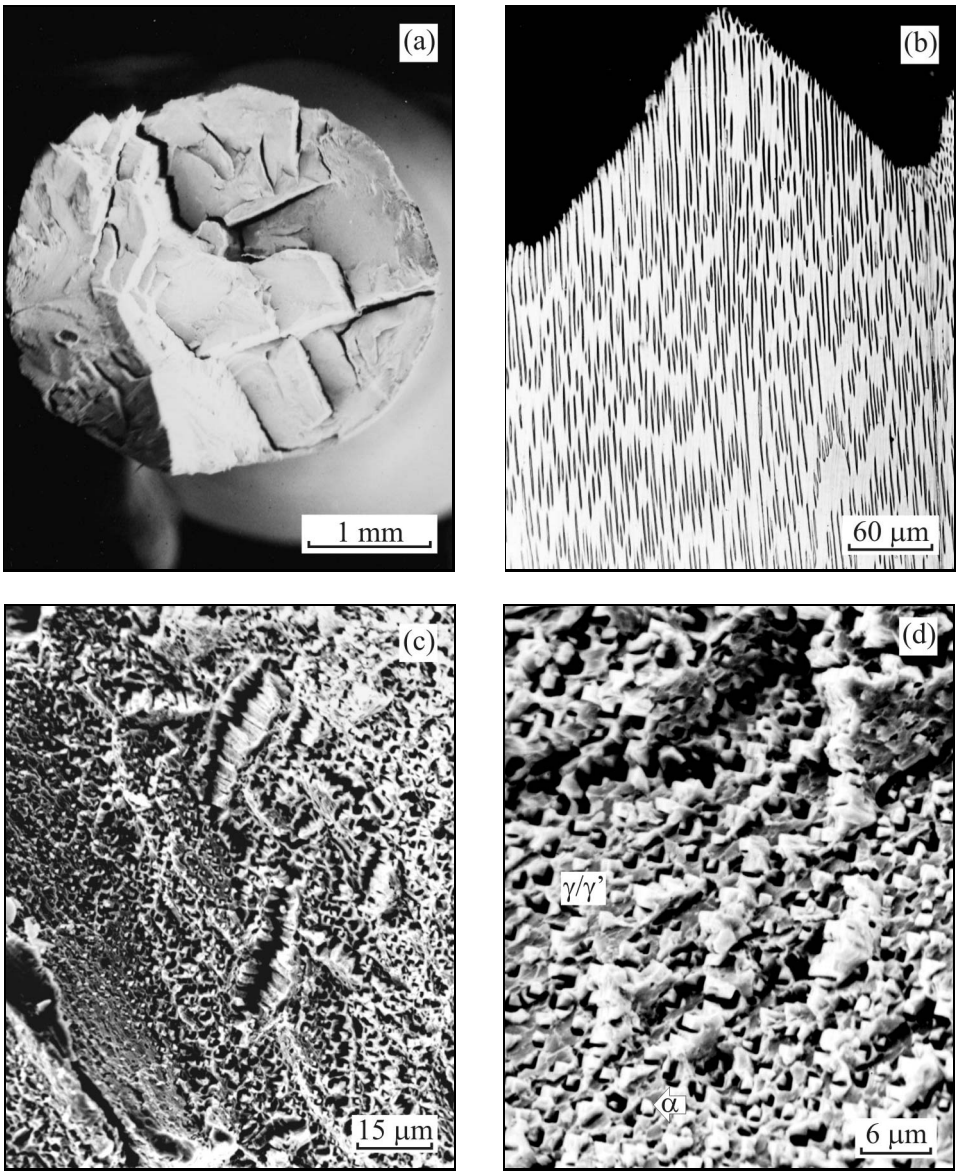

Fig. 7. Typical fracture features of the Alloy 1, $R = 4.17 \times 10^{-6}$ m·s^{-1}: (a) SEM micrograph showing fracture surface with the cracks parallel to the tensile axis; (b) OM micrograph of a longitudinal section of the tensile specimen in the vicinity of the fracture surface; (c) SEM micrograph showing ductile fracture of the matrix and fibres; (d) SEM micrograph illustrating pull-out of the fibres from the matrix and cavities formed around the reinforcing phase.

and the fibres show ductile fracture mode associated with a large reduction of fibre cross section area after fracture. The decohesion at the fibres-matrix interfaces causes pull-out of some fibres and formation of deep cavities at the fracture surface (Fig. 7d). As shown by Lapin [14] using in-situ straining of in-situ composite in SEM, multiple slip systems operate in the γ/γ'-matrix. The dislocations on the $\{111\}$ slip planes and in the $\langle 110\rangle$ slip directions in the γ/γ'-matrix, nucleate dislocations on the $\{110\}$ slip planes in the $\langle 111\rangle$ slip directions of the fibres [24]. In spite of high local plastic deformation in the necked region of the specimens, the fibres deformed plastically without any evidence for cracking and fragmentation [14]. Different slip systems operating in the matrix and fibres and high pile-up stresses initiated voids at the fibre-matrix interfaces [14], which were similar to those observed in the present study.

4. Conclusions

The investigation of the effect of the growth rate on the microstructure and room-temperature tensile properties of DS Ni_3Al-based in-situ composites yielded the following conclusions:

1. The microstructure of DS in-situ composites consisted of α-Mo fibres in the γ/γ'-matrix. The interfibre spacing λ varied with the growth rate R according to the relationship $\lambda = K_1 R^{-0.5}$, where a material constant K_1 for both alloys is determined to be 4.44×10^{-9} $\mathrm{m^{1.5}\cdot s^{-0.5}}$.

2. The growth rates of 6.94×10^{-6} and 8.33×10^{-6} $\mathrm{m\cdot s^{-1}}$ are found to be critical for a planar front solidification at a constant temperature gradient of $G_\mathrm{L} = 15 \times 10^3$ $\mathrm{K\cdot m^{-1}}$ for the Alloy 1 and Alloy 2, respectively. At higher growth rates, a breakdown of planar front solidification accompanied by the growth of irregular eutectic structure is observed. The value of the criteria for plane front solidification $(G_\mathrm{L} R^{-1})_\mathrm{crit}$ is calculated to be 21.6×10^8 and 18×10^8 $\mathrm{K\cdot s\cdot m^{-2}}$ for the Alloy 1 and Alloy 2, respectively.

3. For the composites with a perfect aligned fibre structure, the yield stress increases with increasing growth rate. Formation of cellular structure results in a decrease of the yield stress and ultimate tensile strength. A microstructural model based on a concept of Orowan stress for prediction of the offset yield stress is proposed.

4. During room-temperature tensile testing the composites showed ductile fracture mode. Numerous cracks parallel to the stress axis of the specimens are formed. The decohesion at the fibres-matrix interfaces causes pull-out of some fibres and formation of deep cavities at the fracture surface.

Acknowledgements

This article is dedicated to Prof. RNDr. Pavel Lukáč, DrSc., Dr.h.c. from the Department of Metal Physics of Mathematical and Physical Faculty of Charles University in Prague on the occasion of his 70^{th} birthday. The authors gratefully acknowledge the financial support of the Slovak Grant Agency for Science under the contract VEGA 2/4166/24.

The first author (J. Lapin) on behalf of the Editorial Office of the scientific journal Kovove Materialy-Metallic Materials thanks to Prof. RNDr. Pavel Lukáč, DrSc., Dr.h.c. for his significant scientific contribution represented by 25 scientific papers published in the journal during last 10 years, numerous reviews of the manuscripts, continuous support of the editorial work and wide propagation of the journal in the scientific community.

REFERENCES

[1] CAHN, R. W.: Phil. Trans. R. Soc. Lond., *A351*, 1995, p. 497.
[2] LAPIN, J.: Kovove Mater., *40*, 2002, p. 209.
[3] VAŇO, A.—PELACHOVÁ, T.: Kovove Mater., *42*, 2004, p. 121.
[4] LAPIN, J.: Scripta Mater., *51*, 2004, p. 733.
[5] IŽDINSKÝ, K.—IVAN, J.—ZEMÁNKOVÁ, M.—CSUBA, A.—MINÁR, P.—IŽDINSKÁ, Z.: Kovove Mater., *42*, 2004, p. 316.
[6] IŽDINSKÝ, K.—DUFEK, J.—IVAN, J.—ZEMÁNKOVÁ, M.—MINÁR, P.—IŽDINSKÁ, Z.: Kovove Mater., *41*, 2003, p. 365.
[7] FLORIAN, M.: Kovove Mater., *41*, 2003, p. 73.
[8] WHITTENBERGER, J. D.—NOEBE, R. D.—JOSLIN, S. M.—OLIVER, B. F.: Intermetallics, *7*, 1999, p. 627.
[9] FERRANDINI, P.—BATISTA, W. W.—CARAM, R.: J. Alloys Comp., *381*, 2004, p. 91.
[10] ISHII, T.—DUQUETTE, D. J.—STOLOFF, N. S.: Acta Metall., *29*, 1981, p. 1467.
[11] KOVÁČOVÁ, K.—IVAN, J.: Kovove Mater., *25*, 1987, p. 551.
[12] KOVÁČOVÁ, K.—IVAN, J.—PELACHOVÁ, T.: Kovove Mater., *30*, 1992, p. 463.
[13] PELACHOVÁ, T.—KOVÁČOVÁ, K.: Kovove Mater., *31*, 1993, p. 554.
[14] LAPIN, J.: Int. J. Mater. Prod. Technol., *18*, 2003, p. 255.
[15] LAPIN, J.: J. Mater. Sci. Lett., *15*, 1996, p. 2158.
[16] LAPIN, J. – IVAN, J.: Scripta Metall. Mater., *33*, 1995, p. 391.
[17] LAPIN, J.: Kovove Mater., *34*, 1996, p. 265.
[18] LAPIN, J.: Kovove Mater., *35*, 1997, p. 43.
[19] LAPIN, J.—ONDRÚŠ, Ľ.—NAZMY, M.: Intermetallics, *10*, 2002, p. 1019.
[20] THOMPSON, E. R.—LEMKEY, F. D.: Metall. Trans., *1*, 1970, p. 2799.
[21] JACKSON, K. A.—HUNT, J. D.: AIME Trans., *236*, 1966, p. 1129.
[22] WHITTENBERGER, J. D.—WIRTH, G.: Metal Sci., *16*, 1982, p. 383.
[23] RINALDI, M. D.—SHARP, R. M.—FLEMINGS, M. C.: Metall. Trans., *3*, 1972, p. 3139.
[24] LAPIN, J.—DELANNAY, F.: Metall. Mater. Trans. A, *26A*, 1995, p. 2053.
[25] DALAL, R. P.—THOMAS, C. R.—DARDI, L. E.: In: Proc. Conf. of Superalloys. Eds.: Kell, M., Kortovich, C. S., Kemp, W. B., Bricknell, R. H., Radavich, J. F. Warrendale, Philadelphia, Metallurgical Society of AIME 1984, p. 185.
[26] THORNTON, P. H.—DAVIES, R. G.—JOHNSTON, T. L.: Metall. Trans., *1*, 1970, p. 207.

[27] STOLOFF, N. S.—SIKKA, V. K.: Physical Metallurgy and Processing of Intermetallic Compounds. New York, Chapman & Hall 1996, p. 159.
[28] MULFORD, R. A.—POPE, D. P.: Acta Metall., *21*, 1973, p. 1375.
[29] FLINN, P. A.: AIME Trans., *218*, 1960, p. 145.
[30] DAI, J. Y.—LI, D. X.—YE, H. Q.—JIN, Z. X.—ZHANG, J. H.: J. Mater. Sci., *30*, 1995, p. 248.
[31] DAI, J. Y.—LI, D. X.—YE, H. Q.—JIN, Z. X.—ZHANG, J. H.: J. Mater. Sci., *30*, 1995, p. 253.